

The type-I antiferromagnetic Weyl semimetal InMnTi₂

Davide Grassano* and Luca Binci

*Theory and Simulations of Materials (THEOS), and National Center for Computational Design and Discovery of Novel Materials (MARVEL),
École Polytechnique Fédérale de Lausanne, CH-1015 Lausanne, Switzerland*

Nicola Marzari

*Theory and Simulations of Materials (THEOS), and National Center for Computational Design and Discovery of Novel Materials (MARVEL),
École Polytechnique Fédérale de Lausanne, CH-1015 Lausanne, Switzerland and
Laboratory for Materials Simulations (LMS), Paul Scherrer Institut (PSI), CH-5232, Villigen PSI, Switzerland*

Topological materials have been a main focus of studies in the past decade due to their protected properties that can be exploited for the fabrication of new devices. Among them, Weyl semimetals are a class of topological semimetals with non-trivial linear band crossing close to the Fermi level. The existence of such crossings requires the breaking of either time-reversal (T) or inversion (I) symmetry and is responsible for the exotic physical properties. In this work we identify the full-Heusler compound InMnTi₂, as a promising, easy to synthesize, T - and I -breaking Weyl semimetal. To correctly capture the nature of the magnetic state, we employed a novel DFT + U computational setup where all the Hubbard parameters are evaluated from first-principles; thus preserving a genuinely predictive *ab initio* character of the theory. We demonstrate that this material exhibits several features that are comparatively more intriguing with respect to other known Weyl semimetals: the distance between two neighboring nodes is large enough to observe a wide range of linear dispersions in the bands, and only one kind of such node's pairs is present in the Brillouin zone. We also show the presence of Fermi arcs stable across a wide range of chemical potentials. Finally, the lack of contributions from trivial points to the low-energy properties makes the materials a promising candidate for practical devices.

I. INTRODUCTION

Topological semimetals¹ constitute a class of materials where protected band crossings occur. They can be distinguished as either Dirac² or Weyl semimetals (WSs)^{3,4}, when the crossings happens at isolated points in the Brillouin zone (BZ), or nodal line semimetals⁵, when the crossings span an entire line. For the former case, the crossings, also called nodes, can be assigned to be Dirac or Weyl with a $k \cdot p$ framework, which can take the form of either a Dirac or a Weyl Hamiltonian. The former describes a fourfold degenerate crossing with no chirality, while the latter describes a pair of twofold degenerate crossings with opposite chiralities, as guaranteed by the fermion doubling theorem⁶. The presence of these nodes lead to the emergence of quasi-particle excitations with a behavior similar to that of a Dirac or Weyl fermion⁷, respectively. The focus of this paper is on WSs, which exhibit a wide range of interesting properties such as the Adler-Bell-Jackiw anomaly^{8,9} related to the observation of negative magneto-transport¹⁰⁻¹³, and the presence of atypical surface states known as Fermi arcs³. WSs have been proposed for many applications ranging from the realization of q-bits¹⁴, to Veselago lenses¹⁵ and lasing¹⁶.

One of the main requisites for the realization of a WS is the breaking of either time-reversal (T) or inversion (I) symmetry. If both are present at the same time, it can be shown that two nodes with opposite chirality will always be degenerate, giving rise to a four-fold crossing with zero Chern number. A major breakthrough in the

study of WSs was achieved with the experimental realization of the I -breaking TaAs^{17,18} and the other transition-metal monpnictides^{19,20}. Unfortunately, these materials also display a complex band-structure landscape that can obfuscate the Weyl properties. This can happen due to several features, from the proximity of two neighboring nodes in the same pair which causes a distortion of the expected linear dispersion, to the presence of trivial points²¹. In the search for possible WSs also several T -breaking materials have been proposed, such as the pyrochlore iridates³, antiferromagnetic (AFM) Mn₃Sn and Mn₃Ge^{22,23}, or a promising family of cobalt-based Heusler compounds^{24,25}. In T -breaking WSs, the restriction of having Weyl nodes (WNs) appearing in multiples of 4 is lifted, and the number of pairs present can range from a single to multiple ones. Recently, an interesting paradigm in the design of WSs has been proposed with the introduction of the ferromagnetic (FM) ternary compounds RAlX [R = rare earth, X=Ge,Si]²⁶, like CeAlSi²⁷, where both T and I symmetries are broken. In this case the material can be seen as an I -breaking WS with a Zeeman-like perturbation that causes a shift in the position of the nodes depending on their Chern number. These materials have the same crystal structure as the transition-metal monpnictides, and indeed exhibit the same 4/8 pairs of W1/2 nodes, shifted depending on their Chern number and, in some cases, depending on the material composition, also additional W3 and W4 nodes, always organized in $4n$ pairs.

In this letter we perform a systematic study of

the properties of InMnTi₂, a non-centrosymmetric full-Heusler compound²⁸ belonging to space group 216. Among several possible spin configurations, we predict that the AFM phase is the most stable one. As alluded to above, we expect to find Weyl nodes organized in $4n$ pairs with a Zeeman-induced shift in their positions depending on the node's Chern number. Indeed, in the present analysis, we find 12 pairs of type-I nodes²⁹ throughout the entire BZ of the material, which are all equivalent modulus a minor shift in k -space induced by the AFM phase. We show that in InMnTi₂ the distance between a pair of neighboring nodes is greater than that in I -breaking WSSs such as the transition-metal monpnictides, and greater or comparable to that of T -breaking ones, while still being very close to the Fermi level. Finally, we also show that only a trivial pocket of electrons is present at Γ in addition to the Fermi pockets given by the WNs, and its contribution is negligible to the Weyl properties, as shown in the computed density of states (DOS) and optical properties.

II. METHODS

Density-functional theory (DFT) calculations have been carried out using the open-source **Quantum ESPRESSO**^{30,31} distribution in combination with the norm-conserving full-relativistic pseudopotentials from the ONCVSP library³², with the exchange and correlation functional derived within the Perdew, Burke and Ernzerhof generalized-gradient approximation³³. The parameters and convergence thresholds set for the calculations are higher than conventional ones, in order to guarantee an accuracy of the order of 1 meV for the resulting band eigenvalues. In particular, we use a plane wave cutoff for the wavefunctions \mathbf{G} -vectors of 150 Ry. The initial relaxation and self-consistent calculations are carried out using a $9 \times 9 \times 9$ Monkhorst-Pack mesh to sample the BZ. Successively, a non self-consistent calculation with a $12 \times 12 \times 12$ grid has been used to perform the Wannierization of the wavefunctions with Wannier90³⁴. In order to determine the magnetic configuration of the material, several supercells have been considered with different starting spin configurations. To account for the localized nature of $3d$ electrons in transition-metals, we employed the fully relativistic noncollinear parametrization of Dudarev's DFT + U functional^{35,36}. The internal consistency and the predictive character of the method are guaranteed by directly evaluating the Hubbard parameters for the Ti- $3d$ and Mn- $3d$ states also including spin-orbit coupling. To do this, we used the linear response³⁷ density-functional perturbation theory approach^{38,39}, that we recently generalized to the non-collinear fully relativistic case⁴⁰. In this scheme, the Hubbard U correction is given by $U^I = (\chi_0^{-1} - \chi^{-1})_{II}$, where the interacting (noninteracting) response matrix χ (χ_0) are given by the curvature of the total energy with respect to an external field constraining the

$3d$ orbital occupation: $\chi_{II} = \sum_i^{\text{occ}} (\langle \Psi_i | P^I | \delta_I \Psi_i \rangle + \langle \mathcal{T} \Psi_i | \mathcal{T} P^I \mathcal{T}^\dagger | \mathcal{T} \delta_I \Psi_i \rangle)$. The linearized perturbed wavefunctions satisfy two Sternheimer equations; a standard and a time-reversed one⁴⁰:

$$(H_{[\mathbf{B}]} - \epsilon_i) |\delta_I \Psi_i\rangle = -\mathcal{P} \delta_I V_{\text{KS}}^{[\mathbf{B}]} |\Psi_i\rangle \quad (1)$$

$$(H_{[-\mathbf{B}]} - \epsilon_i) |\mathcal{T} \delta_I \Psi_i\rangle = -\Pi \delta_I V_{\text{KS}}^{[-\mathbf{B}]} |\mathcal{T} \Psi_i\rangle \quad (2)$$

where \mathbf{B}_{xc} is the magnetic exchange correlation potential. With this method, using a $4 \times 4 \times 4$ \mathbf{q} -points mesh, we estimated $U = 2.45$ eV for the Mn- $3d$ and $U = 2.27$ eV for the Ti- $3d$ states.

The bands used for the Wannierization have been chosen so as to include the entire isolated manifold including both the valence and conduction bands around the Fermi level. Following the Wannierization, WannierTools⁴¹ has been employed to perform a Wannier interpolation on a denser $151 \times 151 \times 151$ k -point mesh, and to find the position of all points with a gap smaller than 0.5 meV. The position of the crossings has then also been verified with direct DFT calculations. The denser grids from WannierTools have been used for the calculation of the Fermi surface and DOS. The iterative Green's function method^{42,43} is used in order to compute the surface states on a tetragonal supercell. The surface is cut along the [001] direction and the states are computed both for the Ti/Mn- and Ti/In-terminated surfaces

The Berry curvature Ω defined as the curl of the Berry connection (A)

$$A_n(\mathbf{k}) = i \langle u_{n\mathbf{k}} | \nabla_{\mathbf{k}} | u_{n\mathbf{k}} \rangle. \quad (3a)$$

$$\Omega_n(\mathbf{k}) = \nabla_{\mathbf{k}} \times A_n(\mathbf{k}) \quad (3b)$$

has been computed using WannierBerri⁴⁴. The Chern number of the nodes has been computed both by considering the flux of $\Omega_n(\mathbf{k})$ on a sphere surrounding the node (4), and using **Z2pack**⁴⁵ to track the evolution of the hybrid Wannier charge centers (HWCCs) on a sphere surrounding each node.

$$C = \int_{\text{BZ}} d\mathbf{S} \cdot \Omega_n(\mathbf{k}) \quad (4)$$

The optical conductivity of the material has been computed within the independent-particle approach⁴⁶ using the Kubo-Greenwood formula as implemented in Wannier90. The diagonal elements of the real part of the optical conductivity are given by^{47,48}

$$\sigma_{1,jj}(\omega) = \frac{2\pi e^2}{m^2 \omega V} \sum_{\mathbf{k}} \sum_{c,v} [f(\epsilon_v(\mathbf{k})) - f(\epsilon_c(\mathbf{k}))] \times |\langle c\mathbf{k} | p_j | v\mathbf{k} \rangle|^2 \delta(\epsilon_c(\mathbf{k}) - \epsilon_v(\mathbf{k}) - \hbar\omega) \quad (5)$$

where V is the cell volume and v and c are the valence and conduction bands indexes respectively. In order to ensure that the optical properties are converged within a broadening of 3 meV, we perform the calculation on a

set of increasingly denser k -points meshes up to a $300 \times 300 \times 300$ grid, where the convergence criteria is satisfied. The imaginary part of the dielectric tensor can be derived from the optical conductivity using the formula

$$\text{Im } \varepsilon_{jj}(\omega) = \frac{4\pi}{\omega} \text{Re } \sigma_{jj}(\omega) \quad (6)$$

The entire process has been automated with AiiDA^{49,50} workflows, which let us keep track of the metadata and provenance for every step of the calculation. The relative plugins for QE and Z2pack have also been employed.

III. RESULTS AND DISCUSSIONS

InMnTi₂ has been selected from a high-throughput screening performed on materials derived from the ICSD and COD databases, in which the material was previously identified as a Weyl semimetal with a non-magnetic ground state^{51,52}. When testing magnetic configurations, even when considering supercells, the non-magnetic one is always the most energetically favored at the PBE level. On the contrary when including Hubbard corrections, the non-magnetic state becomes metastable, and the lowest energy state becomes the AFM one in the primitive cell, where the in which the Ti and Mn atoms form 2 sublattices with opposite spin configuration. The cell parameter derived from the relaxation is the same as that of the original screening of 3.134 Å.

It is worth noting that the material has also been predicted to be a WS by chemical substitution and study of the anomalous Nernst effect by Noky et al.⁵³, starting from the work of Shi et al.⁵⁴, in which they study an equivalent inverted Heusler compound Ti₂MnAl. It should be stated that for this material they obtain the antiferromagnetic configuration as the most stable one, with opposite spin directions on Ti and Mn sublattices, already at the PBE level.

The band dispersion of the material in the antiferromagnetic configuration is shown in Fig. 1a, from which several features can be observed. Several bands are crossing at the Γ point, which results in the presence of a trivial pocket in the Fermi surface (Fig. 1b). Also, a direct gap can be observed along the $\Gamma \rightarrow K$ direction, which is a direct consequence of the presence of a pair of WNs in its proximity. Across the entire BZ, 12 pairs of WNs can be identified, as shown in Fig. 1c. All the nodes can be mapped to a single node position $k_W = (0.2361, 0.3712, 0.0000)$ 96 meV below the Fermi level, plus a Chern and K dependent momentum shift, as expected from an I and T breaking Weyl semimetal. The difference between the band structure and node positions between the DFT+U AFM results and the non-magnetic PBE ones is shown in the supplementary material (see Fig. SM2 and SM3). Notably, the shift for the nodes in the $k_z = 0$ plane is of 0.0047 \AA^{-1} along the k_z direction with sign opposite to the Chern number of the node (see

Fig. 1). The energy of the nodes also remain the same within the accuracy of 1 meV.

We then compute the band dispersion along the line connecting two adjacent WNs ($W \rightarrow W$) _{x} and two direction y and z perpendicular to it and to each other, with y belonging to the xy plane (see Fig. 2). This has been performed both in DFT and with Wannier interpolations, in order to show that the Wannier function are able to reproduce the band dispersions of the nodes with a 1 meV accuracy. When dealing with pair of nodes, we are interested in the distance between each other as it is tied to the linear range of the band dispersion and hence the strength of the Weyl character of the nodes. The separation between nodes is also directly related to the possible strength of the quantum Hall effect (QHE) in the Weyl semimetal⁵⁵. In the case of the node pairs in InMnTi₂ their distance is 0.37 \AA^{-1} which is roughly four times the spacing present in the W2 nodes of TaAs and 10 time that of the W1 ones⁵⁶. This large distance for a pair means that the linear dispersion of a single node holds for a range of 60 meV, allowing for the low-energy properties tied to the Weyl fermion picture to clearly manifest themselves in the material. Another two parameters that can be derived from the dispersion are the Fermi velocity tensor and the tilt vector²¹. The latter can also be used to classify the WN as of type-I or II²⁹. Using this analysis for InMnTi₂ we observe that the nodes are of type-I, given that the tilt of the node is not strong enough. The fact that the nodes are of type-I can also be seen by observing the plot of the Fermi surface in Fig. 1b, where closed electron pockets are clearly visible around each pair of nodes. Also a trivial hole pocket is present around Γ , as expected from the band structure. We show in the later discussion of the DOS and optical properties that the presence of this trivial pocket does not give a noticeable contribution to the low-energy properties of the material, in contrast to other WSs like the transition-metal monpnictides²¹. We also hypothesize that band structure engineering such as strain, electric field or doping could be used to bring the bands at Γ below the Fermi level while not altering the topology of the material⁵⁷. By analyzing the DOS around the node position E_W (see Fig. 3), we can show that the presence of the trivial pocket at Γ will have a negligible contribution to the Weyl properties. Indeed, given a three-dimensional WN, the expected behavior of the DOS should be $D(E) \sim (E - E_W)^{2/3}$ in a region around E_W . We show that it is possible to perform a quadratic fit around the node position (inset of Fig. 3), in the same range as the linearity range derived from the node band dispersion, with a p-value greater than 0.99. The only deviation from the ideal behavior is that the DOS does not go exactly to zero at E_W , as a consequence of the presence of the trivial pocket at Γ . The fact that the low-energy properties are perfectly compatible with a Weyl fermion picture can also be observed from the optical conductivity, shown in Fig. 4b. For a type-I WN the real part of the optical conductivity is expected to have a linear

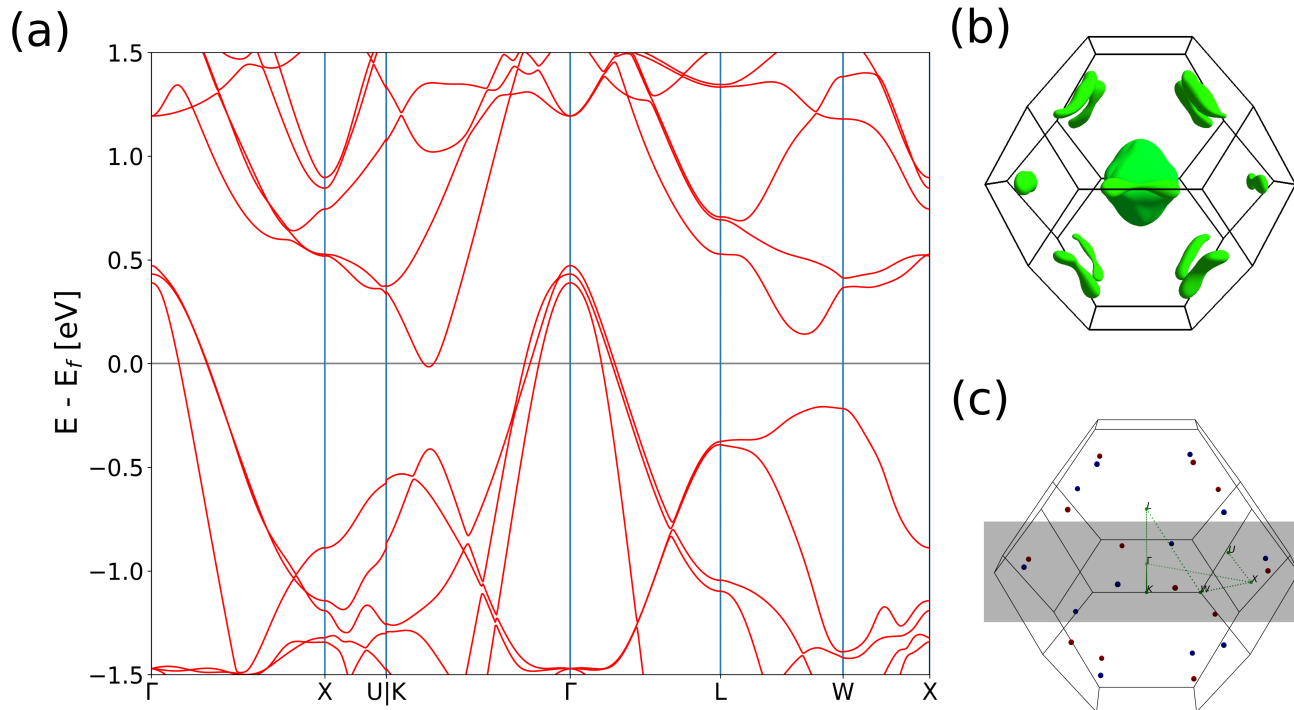


FIG. 1. (a) Band structure along the high-symmetry path. (b) Plot of the Fermi surface obtained from a Wannier interpolation on a $151 \times 151 \times 151$ k-point grid. The Fermi surface shows pockets surrounding the 12 pairs of WNs. Only one other pocket of trivial points is present around Γ . (c) Plot of the BZ including the position of the WNs in the antiferromagnetic ground state. The nodes with chirality +1 are shown in red, while the one with chirality -1 are shown in blue. The green lines show the high-symmetry path on which the bands have been calculated.

dispersion in the low energy range ($\omega \rightarrow 0$), starting from an onset of $2E_W$ due to the WNs not being exactly aligned with the Fermi level⁵⁶. In Fig. 4b we show that a linear fit can be performed starting from an onset of 150 meV. This value is slightly lower than the expected 192 meV due to the slight anisotropy of the WN dispersion along the $k_{(W \rightarrow W)_y}$; still we observe a linear dispersion of the optical conductivity in a range wider than the expected 60 meV.

We then proceed to compute the surface states of the material, for a tetragonal supercell cut along the [001] direction. The spectral function of both the Ti/Mn- and Ti/In-terminated surfaces along the high-symmetry lines of the surface BZ are shown in Fig. 5a. A clear distinction between the bulk and the surface states can be inferred by the intensity of the plots. In Fig. 5b we compute the same quantity along the direction connecting the projection of two Weyl nodes with opposite chirality. Here we can observe the projection of the same bulk states that are also shown in Fig. 2, plus a surface band leaking from one bulk node into the other which is directly related to the Fermi arcs. Finally, in Fig. 5c we show a plot of the 2D Fermi surface at the chemical potential of $\mu = -0.96$ meV, corresponding to the position of the WNs. As expected, we observe the presence of open lines commonly known as "Fermi arcs" connecting the

projections of the pair of nodes, highlighted in the figure with red/blue dots. The Fermi arcs are clearly defined, being separated from the bulk states, and can be longer than 1 \AA^{-1} , which should make them easily detectable experimentally. The presence of seemingly double arcs in the Ti/In-terminated surface is due to the overlap of the projections 2 nodes at the $\pm k_z$ positions. The movies provided as supplementary materials also show the evolution of the arcs shape by varying the chemical potential from -100 to 0 meV. From this we can see that the arcs remain stable across a wide range of chemical potentials, even when the Fermi pockets around the nodes, or other trivial surface states start to interact/cross with them.

Finally, we compute the Berry curvature by means of Wannier interpolation on a dense regular grid of k-points. We can then interpolate the value of the Berry curvature on a custom grid, such as a sphere around a WN which can then be used to derive the Berry curvature flux, the integral of which (4) will give the Chern number associated with the node. The analysis shows that two neighboring nodes belonging to a pair are of opposite chirality, as we would expect. The results from the study of the evolution of the HWCCs corroborates the previous results, showing that the two nodes are of chirality +1 and -1 respectively. We also show in Fig. 6 the Berry curvature computed on the $k_z = 0$ plane in proximity of

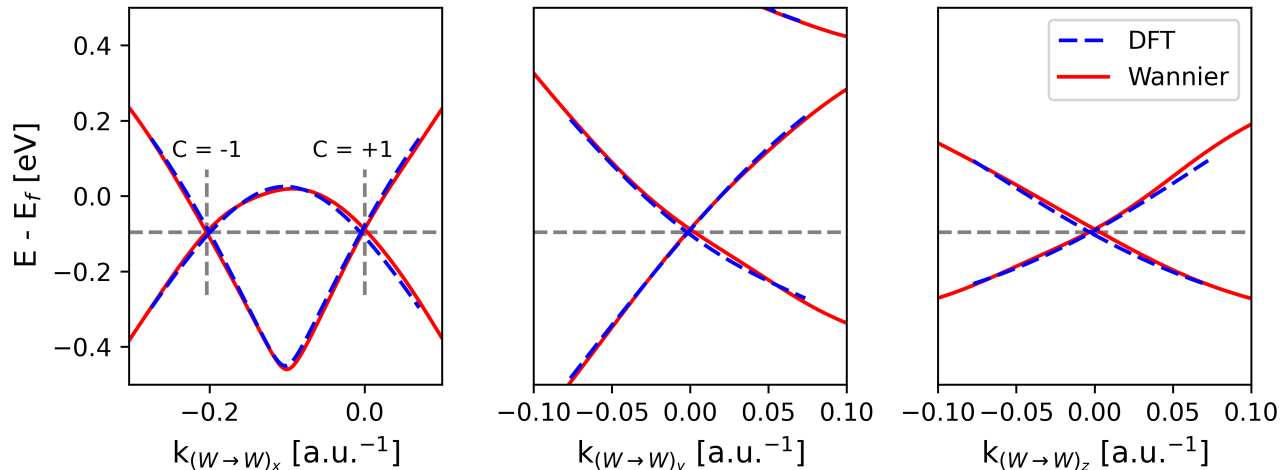


FIG. 2. Plot of the DFT (dashed blue) and Wannier (red) band dispersion in proximity of a Weyl node. The $W \rightarrow W$ x direction is set to line that joins a pair of adjacent Weyl nodes. The y and z directions are chosen to be perpendicular to x and each other with y laying in the xy plane.

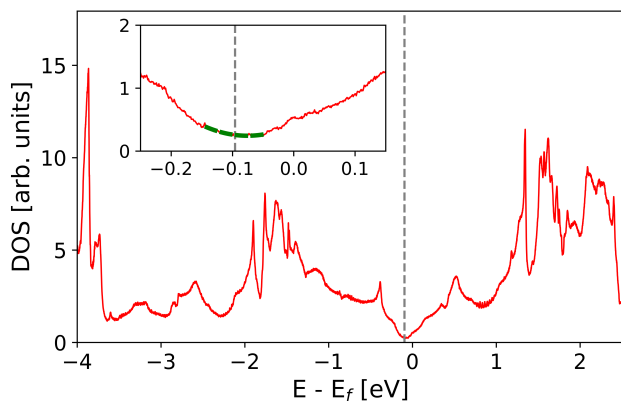


FIG. 3. Plot of the DOS near the Fermi level computed from a Wannier interpolation on a $151 \times 151 \times 151$ k-point grid with a gaussian smearing of 1 meV. The inset shows a zoom in an energy range closer to the Fermi level; in green is the fit of the DOS near the WN using a quadratic polynomial for the expected 60 meV range. The DOS has a minimum at -0.096 meV which is the expected position of the WNs with respect to the Fermi level. The fact that the DOS does not go to zero is the consequence of the presence of the pocket at Γ , but the expected quadratic behavior is still clearly present.

a pair of WNs; while the general trend shows the Berry curvature going from the $C = +1$ node to the $C = -1$ one, this is not universally true as one would expect from an ideal pair model²¹.

IV. CONCLUSIONS

In conclusion we suggest that InMnTi_2 is a type-I antiferromagnetic Weyl semimetal with properties that would make it an excellent candidate for future experimental studies of low-energy Weyl fermion physics, due to the presence of only one kind of Weyl point with excellent pair separation and linearity range. We also show that, even if a trivial pocket is present at Γ , it does not contribute significantly to the low-energy properties, and could furthermore be eliminated via material band engineering. These characteristic reflects on the quality of the observable surface states. In particular, we predict the presence of Fermi arcs that are clearly defined, with a length of over 1 \AA^{-1} , and well separated from the bulk states on a wide range of chemical potentials.

V. ACKNOWLEDGEMENTS

This research was supported by the NCCR MARVEL, a National Centre of Competence in Research, funded by the Swiss National Science Foundation (grant number 182892).

VI. COMPETING INTERESTS

The Authors declare no Competing Financial or Non-Financial Interests.

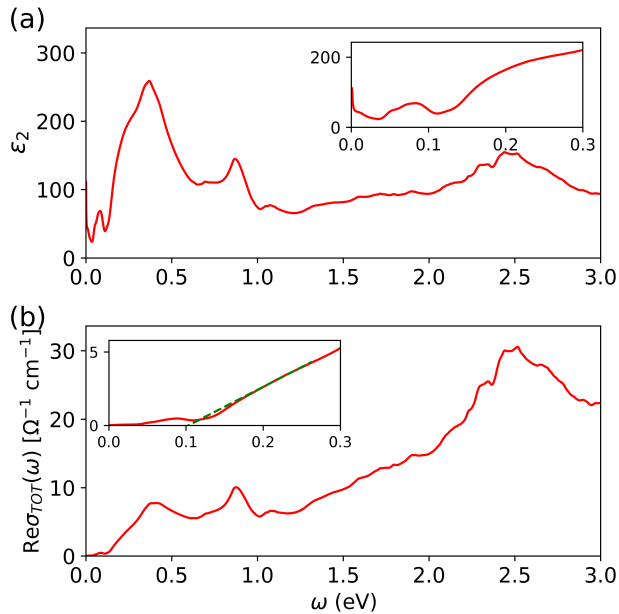


FIG. 4. (a) Plot of the computed imaginary part of the dielectric function. (b) Plot of the real part of the optical conductivity. In green, the results of the linear fit starting from the onset energy given by $2E_w$. The plots show that the low-energy excitation properties fully agree with the model for a type-I WS. Indeed, we observe that real part of the optical conductivity can be fitted with a linear dispersion starting from an onset of 150 meV in a range wider than the expected 60 meV.

VII. DATA AVAILABILITY

The data supporting the findings of this paper are available on the Materials Cloud⁵⁸ at Ref. 59.

VIII. AUTHOR CONTRIBUTIONS

D.G. is responsible for the conceptualization of the project. D.G. performed the DFT, Wannierization and post-processing calculations. L.B. provided the non-collinear DFT+ U code and performed the DFPT calculations to derive the *ab initio* Hubbard parameters. N.M. supervised the project. All authors contributed to the discussions and writing of the manuscript.

-
- * davide.grassano@epfl.ch
- ¹ N. Armitage, E. Mele, and A. Vishwanath, *Reviews of Modern Physics* **90**, 015001 (2018).
 - ² Z. Wang, Y. Sun, X.-Q. Chen, C. Franchini, G. Xu, H. Weng, X. Dai, and Z. Fang, *Physical Review B* **85**, 195320 (2012).
 - ³ X. Wan, A. M. Turner, A. Vishwanath, and S. Y. Savrasov, *Physical Review B* **83**, 205101 (2011).
 - ⁴ S. Murakami, *New Journal of Physics* **9**, 356 (2007).
 - ⁵ A. Burkov, M. Hook, and L. Balents, *Physical Review B* **84**, 235126 (2011).
 - ⁶ H. Nielsen and M. Ninomiya, *Physics Letters B* **105**, 219 (1981).
 - ⁷ P. B. Pal, *American Journal of Physics* **79**, 485 (2011).
 - ⁸ S. L. Adler, *Physical Review* **177**, 2426 (1969).
 - ⁹ J. S. Bell and R. Jackiw, *Il Nuovo Cimento A* (1965-1970) **60**, 47 (1969).
 - ¹⁰ N. J. Ghimire, Y. Luo, M. Neupane, D. Williams, E. Bauer, and F. Ronning, *Journal of Physics: Condensed Matter* **27**, 152201 (2015).
 - ¹¹ C.-L. Zhang, S.-Y. Xu, I. Belopolski, Z. Yuan, Z. Lin, B. Tong, G. Bian, N. Alidoust, C.-C. Lee, S.-M. Huang, *et al.*, *Nature communications* **7**, 10735 (2016).
 - ¹² F. Arnold, C. Shekhar, S.-C. Wu, Y. Sun, R. D. Dos Reis, N. Kumar, M. Naumann, M. O. Ajeesh, M. Schmidt, A. G. Grushin, *et al.*, *Nature communications* **7**, 11615 (2016).
 - ¹³ J. Gooth, A. C. Niemann, T. Meng, A. G. Grushin, K. Landsteiner, B. Gotsmann, F. Menges, M. Schmidt, C. Shekhar, V. Süß, *et al.*, *Nature* **547**, 324 (2017).
 - ¹⁴ D. Castelvecchi, *Nature News* **547**, 272 (2017).
 - ¹⁵ R. D. Hills, A. Kuznetsov, and F. Kuznetsov, *Physical Review B* **95**, 214103 (2017).
 - ¹⁶ G. Oktay, M. Sarisaman, and M. Tas, *Scientific Reports* **10**, 1 (2020).
 - ¹⁷ S.-M. Huang, S.-Y. Xu, I. Belopolski, C.-C. Lee, G. Chang, B. Wang, N. Alidoust, G. Bian, M. Neupane, C. Zhang, *et al.*, *Nature communications* **6**, 1 (2015).
 - ¹⁸ B. Lv, H. Weng, B. Fu, X. P. Wang, H. Miao, J. Ma, P. Richard, X. Huang, L. Zhao, G. Chen, *et al.*, *Physical Review X* **5**, 031013 (2015).
 - ¹⁹ I. Belopolski, S.-Y. Xu, D. S. Sanchez, G. Chang, C. Guo, M. Neupane, H. Zheng, C.-C. Lee, S.-M. Huang, G. Bian, *et al.*, *Physical Review Letters* **116**, 066802 (2016).
 - ²⁰ Y. Sun, S.-C. Wu, and B. Yan, *Physical Review B* **92**, 115428 (2015).
 - ²¹ D. Grassano, O. Pulci, E. Cannuccia, and F. Bechstedt, *The European Physical Journal B* **93**, 1 (2020).
 - ²² S. Nakatsuji, N. Kiyohara, and T. Higo, *Nature* **527**, 212 (2015).
 - ²³ H. Yang, Y. Sun, Y. Zhang, W.-J. Shi, S. S. Parkin, and B. Yan, *New Journal of Physics* **19**, 015008 (2017).

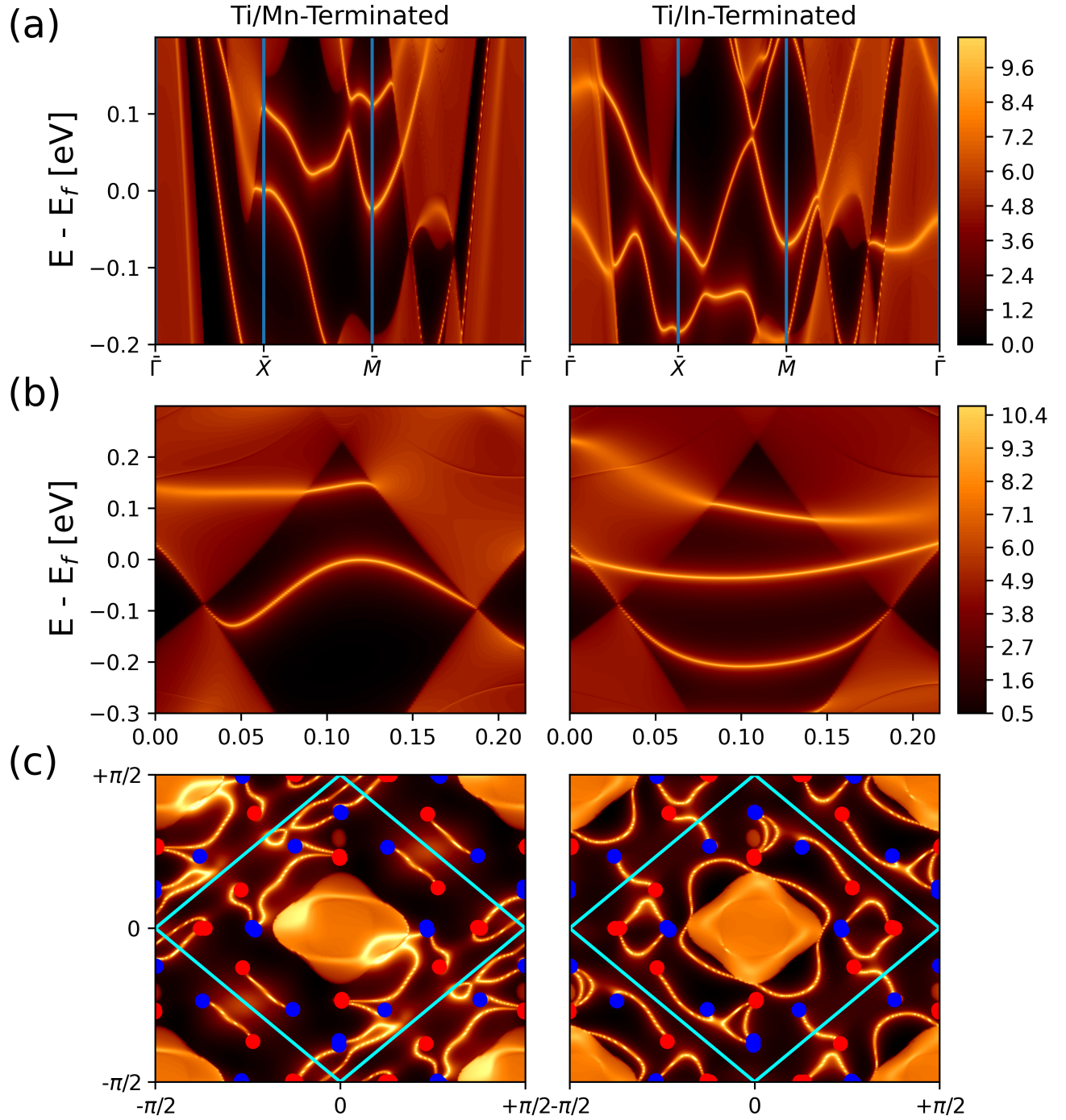


FIG. 5. Surface states computed with the iterative Green's function method on top of the Wannierization for both the titanium and indium terminated surfaces cut along the [001] direction. (a) angular resolved photoemission spectroscopy plot along the high-symmetry path in proximity of the Fermi level (b) angular resolved photoemission spectroscopy plot along the $W \rightarrow W$ direction. The touching point of the Weyl nodes from the bulk states is clearly visible, as well as the more pronounced bands related to the Fermi arcs that joins the 2 nodes. (c) Fermi surface of the surface states computed at $\mu = -0.096$. The red(blue) dots represent the projection of the Weyl nodes with chirality $+1(-1)$. The Fermi arcs going from nodes of opposite chirality can be observed.

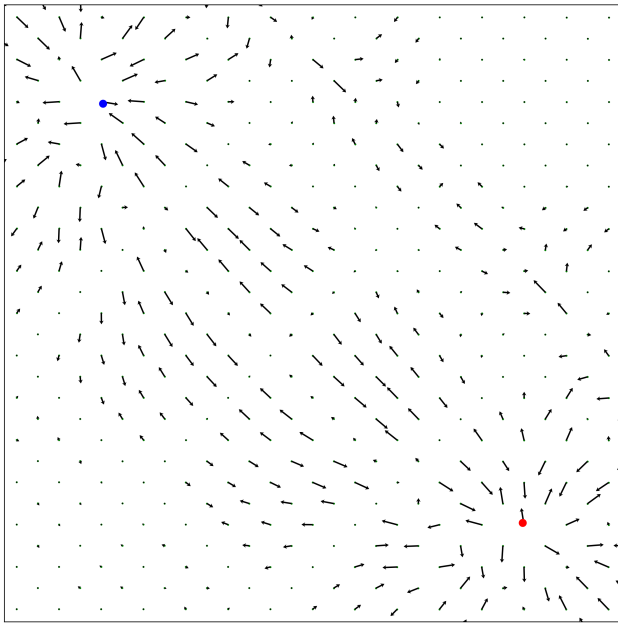


FIG. 6. Plot of the Berry curvature on a $k_z = 0$ plane in proximity of 2 neighboring WNs. The red and blue dots represent a node with chirality +1 and -1 respectively. While the 2D plot highlights only the in-plane components of the Berry curvature, the magnitude along the z axis is also taken into account in order to give a more realistic picture when trying to infer the chirality of a node from the plot.

- ²⁴ Z. Wang, M. Vergniory, S. Kushwaha, M. Hirschberger, E. Chulkov, A. Ernst, N. P. Ong, R. J. Cava, and B. A. Bernevig, *Physical review letters* **117**, 236401 (2016).
- ²⁵ J. Kübler and C. Felser, *EPL (Europhysics Letters)* **114**, 47005 (2016).
- ²⁶ G. Chang, B. Singh, S.-Y. Xu, G. Bian, S.-M. Huang, C.-H. Hsu, I. Belopolski, N. Alidoust, D. S. Sanchez, H. Zheng, *et al.*, *Physical Review B* **97**, 041104 (2018).
- ²⁷ H.-Y. Yang, B. Singh, J. Gaudet, B. Lu, C.-Y. Huang, W.-C. Chiu, S.-M. Huang, B. Wang, F. Bahrami, B. Xu, *et al.*, *Physical Review B* **103**, 115143 (2021).
- ²⁸ T. Graf, F. Casper, J. Winterlik, B. Balke, G. H. Fecher, and C. Felser, *Zeitschrift für anorganische und allgemeine Chemie* **635**, 976 (2009).
- ²⁹ A. A. Soluyanov, D. Gresch, Z. Wang, Q. Wu, M. Troyer, X. Dai, and B. A. Bernevig, *Nature* **527**, 495 (2015).
- ³⁰ P. Giannozzi, S. Baroni, N. Bonini, M. Calandra, R. Car, C. Cavazzoni, D. Ceresoli, G. L. Chiarotti, M. Cococcioni, I. Dabo, A. D. Corso, S. de Gironcoli, S. Fabris, G. Fratesi, R. Gebauer, U. Gerstmann, C. Gougoussis, A. Kokalj, M. Lazzeri, L. Martin-Samos, N. Marzari, F. Mauri, R. Mazzarello, S. Paolini, A. Pasquarello, L. Paulatto, C. Sbraccia, S. Scandolo, G. Sclauzero, A. P. Seitsonen, A. Smogunov, P. Umari, and R. M. Wentzcovitch, *Journal of Physics: Condensed Matter* **21**, 395502 (2009).
- ³¹ P. Giannozzi, O. Andreussi, T. Brumme, O. Bunau, M. B. Nardelli, M. Calandra, R. Car, C. Cavazzoni, D. Ceresoli, M. Cococcioni, *et al.*, *Journal of Physics: Condensed Matter* **29**, 465901 (2017).
- ³² D. Hamann, *Physical Review B* **88**, 085117 (2013).
- ³³ J. P. Perdew, K. Burke, and M. Ernzerhof, *Phys. Rev. Lett.* **77**, 3865 (1996).
- ³⁴ G. Pizzi, V. Vitale, R. Arita, S. Blügel, F. Freimuth, G. Géranton, M. Gibertini, D. Gresch, C. Johnson, T. Koretsune, *et al.*, *Journal of Physics: Condensed Matter* **32**, 165902 (2020).
- ³⁵ S. L. Dudarev, G. A. Botton, S. Y. Savrasov, C. J. Humphreys, and A. P. Sutton, *Phys. Rev. B* **57**, 1505 (1998).
- ³⁶ S. L. Dudarev, P. Liu, D. A. Andersson, C. R. Stanek, T. Ozaki, and C. Franchini, *Phys. Rev. Mater.* **3**, 083802 (2019).
- ³⁷ M. Cococcioni and S. De Gironcoli, *Physical Review B* **71**, 035105 (2005).
- ³⁸ S. Baroni, S. de Gironcoli, A. Dal Corso, and P. Giannozzi, *Rev. Mod. Phys.* **73**, 515 (2001).
- ³⁹ I. Timrov, N. Marzari, and M. Cococcioni, *Phys. Rev. B* **98**, 085127 (2018).
- ⁴⁰ L. Binci and N. Marzari, *Phys. Rev. B* **108**, 115157 (2023).
- ⁴¹ Q. Wu, S. Zhang, H.-F. Song, M. Troyer, and A. A. Soluyanov, *Computer Physics Communications* **224**, 405 (2018).
- ⁴² F. Guinea, C. Tejedor, F. Flores, and E. Louis, *Physical Review B* **28**, 4397 (1983).
- ⁴³ Y.-S. Lee, M. B. Nardelli, and N. Marzari, *Physical review letters* **95**, 076804 (2005).
- ⁴⁴ S. S. Tsirkin, *npj Computational Materials* **7**, 1 (2021).
- ⁴⁵ D. Gresch, G. Autes, O. V. Yazyev, M. Troyer, D. Vanderbilt, B. A. Bernevig, and A. A. Soluyanov, *Physical Review B* **95**, 075146 (2017).
- ⁴⁶ B. Adolph, V. Gavrilenko, K. Tenelsen, F. Bechstedt, and R. Del Sole, *Physical Review B* **53**, 9797 (1996).
- ⁴⁷ F. Bechstedt, *Many-Body Approach to Electronic Excitations. Concepts and Applications* (Springer-Verlag, Heidelberg, 2015).
- ⁴⁸ G. Grosso and G. Pastori Parravicini, *Solid State Physics* (Academic Press, San Diego, 2000).
- ⁴⁹ G. Pizzi, A. Cepellotti, R. Sabatini, N. Marzari, and B. Kozinsky, *Computational Materials Science* **111**, 218 (2016).
- ⁵⁰ S. P. Huber, S. Zoupanos, M. Uhrin, L. Talirz, L. Kahle, R. Häuselmann, D. Gresch, T. Müller, A. V. Yakutovich, C. W. Andersen, *et al.*, *Scientific data* **7**, 300 (2020).
- ⁵¹ D. Grassano, N. Marzari, and D. Campi, (2023), arXiv:2308.01663.
- ⁵² D. Grassano, N. Marzari, and D. Campi, “High-throughput screening of Weyl semimetals,” <https://doi.org/10.24435/materialscloud:na-1b> (2023).
- ⁵³ J. Noky, J. Gayles, C. Felser, and Y. Sun, *Physical Review B* **97**, 220405 (2018).
- ⁵⁴ W. Shi, L. Muechler, K. Manna, Y. Zhang, K. Koepnik, R. Car, J. Van Den Brink, C. Felser, and Y. Sun, *Physical Review B* **97**, 060406 (2018).
- ⁵⁵ K.-Y. Yang, Y.-M. Lu, and Y. Ran, *Physical Review B* **84**, 075129 (2011), publisher: American Physical Society.
- ⁵⁶ D. Grassano, O. Pulci, A. M. Conte, and F. Bechstedt, *Scientific reports* **8**, 1 (2018).
- ⁵⁷ D. Grassano, O. Pulci, V. Shubnyi, S. Sharapov, V. Gusynin, A. Kavokin, and A. Varlamov, *Physical Review B* **97**, 205442 (2018).
- ⁵⁸ L. Talirz, S. Kumbhar, E. Passaro, A. V. Yakutovich, V. Granata, F. Gargiulo, M. Borelli, M. Uhrin, S. P. Huber, S. Zoupanos, *et al.*, *Scientific data* **7**, 299 (2020).

- ⁵⁹ D. Grassano, L. Binci, and N. Marzari, “Prediction of a novel type-I antiferromagnetic Weyl semimetal,” <https://doi.org/10.24435/materialsccloud:ph-3c> (2023).